RSC Advances

PAPER

View Article Online
View Journal | View Issue

Cite this: *RSC Adv.*, 2024, **14**, 26723

Multifunctional silver nanoparticle embedded eri silk cocoon scaffolds against burn wounds-associated infection

Paulami Dam, [a] Shubhajit Shaw, [a] Rittick Mondal, [a] Joydeep Chakraborty, [b] Trinankur Bhattacharjee, [c] Ipsita Kumar Sen, [d] Sanjeet Manna, [e] Abdul Sadat, [a] Supratim Suin, [f] Hironmoy Sarkar, [b] Yavuz Nuri Ertas *[ghi] and Amit Kumar Mandal *[a]

Antimicrobial wound dressings offer enhanced efficacy compared to conventional dressing platforms by limiting bacterial infections, expediting the healing process, and creating a barrier against additional wound contamination. The use of silk derived from silkworm cocoons in wound healing applications is attributed to its exceptional characteristics. Compared to mulberry silk, sericin from non-mulberry cocoons has higher water exchange mobility and moisture retention. Eri, a non-mulberry silkworm, is an unexplored source of silk with an eco-friendly nature of production where the natural life cycle of silkworms is not disrupted, and no moths are sacrificed. This work reports on an eri silk cocoon-based scaffold decorated with silver nanoparticles as a wound dressing material effective against burn-wound-associated multiple-drug-resistant bacteria. The UV-vis spectroscopy showed maximum absorbance at 448 nm due to the surface plasmon resonance of silver nanoparticles. FT-IR spectra exhibited the functional groups in the eri silk proteins accountable for the reduction of Ag^{+} to Ag^{0} in the scaffold. SEM-EDX analysis revealed the presence of elemental silver, and XRD analysis confirmed their particle size of 5.66–8.82 nm. The wound dressing platform showed excellent thermal stability and hydrophobicity, fulfilling the criteria of a standard waterproof dressing material, and anticipating the prevention of bacterial biofilm formation in chronic wounds. The scaffold was found to be effective against both *Staphylococcus aureus* (MTCC 87) and *Pseudomonas aeruginosa* (MTCC 1688) multiple-drug-resistant pathogens. Electron microscopy revealed the bacterial cell damage, suggesting its bactericidal property. The results further revealed that the scaffold was both hemocompatible and cytocompatible, suggesting its potential application in chronic wounds such as burns. As an outcome, this study presents a straightforward, cost-effective, and sustainable way of developing a multifunctional wound dressing platform, suggesting its significant therapeutic potential in clinical and biomedical sectors and facile commercialization.

Received 11th July 2024
Accepted 15th August 2024

DOI: 10.1039/d4ra05029k

rsc.li/rsc-advances

1. Introduction

The skin serves as a vital barrier in the human body, safeguarding organs from environmental variations and microbial invasion.[1] When the skin is injured, numerous complications can occur, such as microbial invasion, increased tissue necrosis, hindered epidermal tissue regeneration, delayed wound healing, and the promotion of scar formation.[2,3] Skin tissue has self-repair abilities; however, big cutaneous wounds are prone to bacterial infection and often do not heal properly. Skin wounds compromise the body's physical defense, making patients vulnerable to life-threatening infections caused by

[a]*Department of Sericulture, Raiganj University, North Dinajpur, 733134, West Bengal, India. E-mail: amitmandal08@gmail.com*
[b]*Department of Microbiology, Cell Biology and Bacteriology Laboratory, Raiganj University, North Dinajpur, 733134, India*
[c]*Department of Conservation Biology, Durgapur Government College, Jawahar Lal Nehru Road, Amarabati Colony, Durgapur, West Bengal, 713214, India*
[d]*Department of Chemistry, Government General Degree College, Salboni, Paschim Medinipur, 721516, West Bengal, India*
[e]*Central Instrumentation Facility, Odisha University of Agriculture and Technology, Bhubaneswar, 751003, Odisha, India*
[f]*Department of Chemistry, Ramakrishna Mission Vivekananda Centenary College, Rahara, Kolkata 700118, India*
[g]*ERNAM-Nanotechnology Research and Application Center, Erciyes University, Kayseri 38039, Turkey. E-mail: yavuznuri@gmail.com*
[h]*Department of Biomedical Engineering, Erciyes University, Kayseri 38039, Turkey*
[i]*Department of Technical Sciences, Western Caspian University, Baku AZ1001, Azerbaijan*

microbes.[4] Burns are the most common and dreadful type of trauma. Based on the World Health Organization 2023 report, burns are responsible for an estimated 180 000 deaths per year, primarily in countries with low and moderate incomes.[5] From 1950 to 2012, the mean total healthcare cost per burn patient was reported to be $88218 (ranging $704–$717,306).[6] Patients with burn injuries tend to survive, yet according to the 2015 United States National Burn Repository, invasive infection and sepsis remain among the top four leading causes of burn morbidity and mortality, accounting for 51% of the deaths.[7] Multiple multidrug-resistant (MDR) bacteria now account for the bulk of these deaths.[8] According to a five-year clinical report, *Pseudomonas aeruginosa* was the leading cause of infection (59%), followed by *Staphylococcus aureus* (17.9%), *Acinetobacter* spp. (7.2%), and *Klebsiella* spp. (3.9%).[9] Post-burn, a competition between proliferating skin cells, *e.g.*, keratinocytes, and colonizing microbes exists for wound dominance.[10] Bacteria have the capability to produce extracellular polymeric substances that protect them against antibiotics, which diminishes their effectiveness.[11] Therefore, it is crucial to develop highly effective antibacterial materials against MDR strains, in addition to screening for new antimicrobials, to check morbidity and mortality rates.[12]

The primary and immediate treatment of burn wounds involves topical antiseptic therapy. Antiseptics, being non-selectively toxic to all biological materials, are detrimental for systemic administration, and microbes can develop resistance against them.[13] Silver agents work well against both Gram-positive and Gram-negative bacteria, despite their drawbacks.[14–17] Silver nitrate or silver sulfadiazine are reported to show cytotoxicity on fibroblasts or keratinocytes, impairing re-epithelialization in burn wounds and often driving blood-related disorders.[18] Hence, alternative strategies for microbial control are needed, where the potential of silver as an antibacterial agent remains imperishable. In this connection, silver nanoparticles (Ag NPs) offer broad-spectrum antimicrobial activity against MDR pathogens, such as *Pseudomonas aeruginosa*.[19] The Center for Disease Control and Prevention has classified the antibiotic-resistant strains linked to it as priority infections, requiring an urgent need to discover new therapeutic strategies. Ag NPs can attack the microbes on multiple cellular targets, thus reducing their chance of becoming resistant.[20,21] The synthesis of Ag NPs involves two approaches, *i.e.*, *in situ* and *ex situ*. *In situ* approach of formation of Ag NPs is more convenient than *ex situ* approaches involving specific reducing agents such as amino acid groups (*e.g.*, carboxylate) residing in silk sericin proteins.[22–24]

Selecting the appropriate dressing material for a wound is crucial. The material should be able to maintain a moist environment, promote epidermal migration and angiogenesis, allow gaseous exchange, maintain tissue temperature, protect against bacterial infections, and be non-adherent, sterile, non-toxic, and non-allergic.[25–27] Traditional clinical dressings like gauze, sterilized cotton, and bandages are cost-effective but provide limited wound healing and infection prevention benefits.[28,29] Thus, to tackle these disadvantages, researchers are exploring silkworm cocoons to address the shortcomings of traditional passive dressings.[30–32]

Cocoons' shielding function is similar to how skin protects our bodies. As a result, the retention of the entire cocoon structure, which includes both fibroin and sericin, may be beneficial for the therapeutic purposes of burns.[33] Silk-fibroin-based protein materials are among the best biomaterials in tissue engineering because of their excellent biocompatibility, bioactivities, and minimal immunogenicity. For instance, dressings made from silk-fibroin can not only assist rapid hemostasis but also enhance the process of healing wounds.[34–36] The cocoon structure has an antimicrobial function, which gives an added advantage for using entire cocoons.[37,38] The cocoon provides a strong protective barrier for the pupa, but it does not prevent the transfer of oxygen or water vapor. Air gaps within cocoons facilitate separate multistage moisture transport processes, resulting in an effective moisture buffer effect.[39,40] The presence of calcium oxalate hydrate crystals on the outer surface of the cocoon obstructs the flow of CO_2 from outside to inside. This indicates that these crystals play a role in capturing a significant amount of CO_2 in the form of hydrogen-bonded bicarbonate on the surface. Entwined silk inside the cocoon structure serves as a second barrier, effectively blocking the flow of residual CO_2. In two extreme natural temperature regimes of 5 °C and 50 °C, the cocoons sustain temperatures from 25 °C to 34 °C, which closely resemble the human body temperature.[41] Therefore, the cocoon mimics the human skin and produces the optimal environment for wound repair and regeneration by allowing preferential CO_2 gating from the internal to the exterior environment while not impeding O_2 and H_2O diffusion, maintaining the correct level of oxygen and moisture content, and promoting speedy wound recovery.[42] Therefore, the microstructural and physiological characteristics of silkworm cocoon inspired the team to merge nanoscience with silk biotechnology to design advanced silver nanocomposites silk cocoon scaffolds (ASN-SCSs) using non-mulberry eri silkworm cocoons.

Eri is a domesticated non-mulberry silkworm (*Philosamia ricini*) under the order Lepidoptera and family *Saturnüdae*. Eri silkworms, unlike *Bombyx mori*, live in a complex external environment and require higher protection.[43] The use of silk fibroin and sericin obtained from wild silkworms has significant potential in the fields of medicine and healthcare. Compared to *Bombyx mori*, *Saturnüdae* silks develop better structural transitions that are well-defined.[44] Compared to mulberry silk, sericin from non-mulberry cocoons has higher water exchange mobility and a high moisture retention capability because of its high hydrophilic to hydrophobic amino acid ratio of 9.06–9.8. Additionally, non-mulberry silk fibroin has distinct arg-gly-asp (RGD) motifs with a favorable cell adhesion effect and better mechanical strength than mulberry silk fibroin.[45,46] Better cell adhesion stimulates tissue growth, cell migration, and signal transmission. As a result, non-mulberry silk would be a suitable choice for preparing silk cocoon scaffolds. Eri cocoons demonstrate distinct multi-stage moisture transmission processes, providing an excellent moisture buffer effect. They also have a slower temperature change inside than

outside, indicating temperature damping capability. The high sericin content of the cocoon coat, along with its exceptional ultraviolet absorption and antibacterial properties, effectively inhibits the infiltration of ultraviolet rays and microbes into the pupae.[47] Understanding the interplay between Eri cocoons' structural properties and performance index can serve as a structural model of bioinspiration in designing or optimizing multifunctional composites that aim to aid the biomedical and public health sectors. Moreover, eri silk, referred to as ahiṁsā (Sanskrit; non-violence) silk or peace silk, was selected due to the eco-friendly nature of production, as the natural life cycle of silkworms was not disrupted and no moth was sacrificed during the experiment.[48]

This study, for the first time, reports the synthesis of the biomimetic advanced silver nanocomposite silk cocoon scaffold (ASN-SCS) bandage, designed using eri silk cocoons, and includes a systematic investigation of its structure, characterization, antibacterial activity, and biocompatibility. An attempt has been made to pave the way for developing an antibacterial dressing material that could combat burn wounds associated with MDR bacterial infection, which, in turn, could stimulate chronic wound healing.

2. Experimental section

2.1 Sample collection

The Eri (*Philosamia ricini*) silkworm cocoons were procured from the office of the Directorate of Textile Sericulture (under the Government of West Bengal), Bogram Sericulture Complex, Raiganj, Uttar Dinajpur, West Bengal.

2.2 Chemical and biological materials

All the chemicals used in this study were of analytical grade. The silver nitrate ($AgNO_3$) was procured from Merck (cat. no. 101512), USA. HiMedia Laboratories, Mumbai, India, provided the bacterial culture media. All the working solutions were made using autoclaved, deionized Milli-Q water. To remove the exogenous DNase or RNase, the glassware was autoclaved for 15 minutes at 121 °C. 70% ethanol was applied to the counter area and all the pipetting devices. Lyophilized *S. aureus* (MTCC 87) and *P. aeruginosa* (MTCC 1688) were obtained from the MTCC, IMTECH Chandigarh, India, and were used following the established safety laboratory protocols.

2.3 Preparation of SCS

SCS was synthesized utilizing non-mulberry Eri cocoons following a slight modification of the method described earlier[49] at a constant temperature of 25 ± 2 °C with a relative humidity of 50 ± 2% in the laboratory setup. Before selecting the cocoon layers for SCS preparation, the terminal portions of silk cocoons and the internal pupal residues were discarded. An Ajisawa solution comprising ethanol, calcium chloride, and H_2O with a molar ratio of 2 : 1 : 8 was prepared. Successively, the prepared cocoon layers were incubated in a water bath at a temperature of 60 °C for 2–3 hours to obtain SCS. After the Ajisawa solution changed color, the prepared cocoons were pulled out and rinsed three times with MilliQ water to acquire SCS samples (Fig. 1).

2.4 Preparation of ASN-SCS

20 mL of $AgNO_3$ aqueous solution with gradients of concentration (Table 1) was added to sterile borosilicate glass Petri plates (diameter 100 mm and height 15 mm), and to reach equilibrium, the SCS was incubated at room temperature and left overnight. The subsequent product was renamed ASN-SCS. Prepared ASN-SCS was taken out and washed three times with MilliQ water for further study.

2.5 Biophysical characterizations

2.5.1 UV-vis and laser light scattering studies. The aqueous Ajisawa solution-mediated synthesis of SCS and $AgNO_3$ aqueous solution-mediated synthesis of ASN-SCS were monitored *via* UV-vis spectrophotometer (Varian Inc., USA) within the wavelength range of 200–800 nm using a quartz cuvette of 1 cm optical path length. The laser diffraction analysis was also conducted for preliminary confirmation of NP formation.

2.5.2 Fourier-transform infrared spectroscopy (FT-IR) analysis. The reactive surface sites on SCS responsible for surface reactivity and the formation of ASN-SCS were detected using Fourier transform infrared (FT-IR) spectroscopy. The infrared spectrum was recorded on the PerkinElmer GX FT-IR system (PerkinElmer, USA) in the 4000–800 cm^{-1} region.

2.5.3 X-ray diffraction (XRD) analysis. The crystallinity characterization of ASN-SCS was obtained by using a Rigaku Miniflex II X-ray diffractometer in the range of 10°–90° at 40 keV operating at 9 kW and CuKα radiation (λ = 1.54056 Å). The X'pert Highscore Plus software was used for processing and analyzing the data. The particle size (d) of the sample was calculated using Scherrer's equation.

2.5.4 Microscopic analysis. The surface morphology of SCS and ASN-SCS was analyzed through a scanning electron microscope (SEM-EDX; S4160 Hitachi, Japan). Before testing, the samples underwent a direct current sputter technique (Emitechk450X, England) to coat them with a thin layer of gold.

2.5.5 Thermogravimetric–differential thermal analysis (TGA/DTA). The thermal properties of ASN-SCS were measured using a thermal gravimetric analyzer (TA instruments, simultaneous TGA–DTA, Waters LLC, New Castle, DE, USA). The tests were conducted under an inert nitrogen atmosphere in an open bin with a heating rate of 10 °C min^{-1} in a temperature range of 25−800 °C. Simultaneously, weight loss and temperature difference between the sample and an inert reference were recorded and plotted against temperature for thermogravimetric analysis (TGA) and differential thermal analysis (DTA), respectively.

2.5.6 Hydrophilicity analysis. The contact angle of a liquid on a fabric's surface is a quantitative measure of the substrate's surface energy. A drop of water was placed on SCS and ASN-SCS to measure the contact angle using the drop deposition method. Images were captured, and the water contact angle measurements were performed using the ImageJ software.

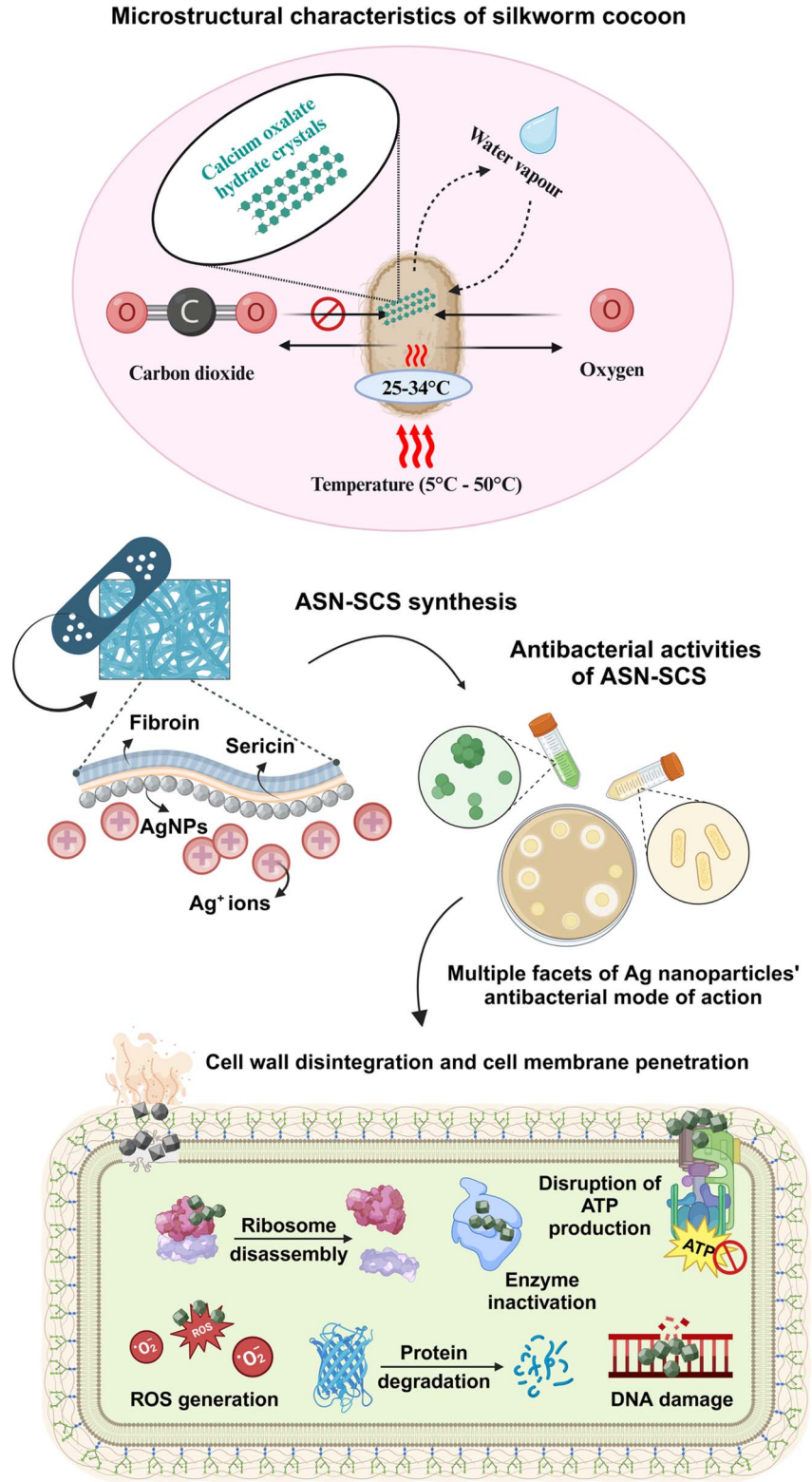

Fig. 1 Microstructural characteristics of a silkworm cocoon and its utility in designing novel ASN-SCS aiding multiple facets of antibacterial mode of action.

2.6 *In vitro* application of ASN-SCS

2.6.1 Kirby–Bauer test or zone of inhibition test. ASN-SCS bandages were tested for their antibacterial efficacy against *P. aeruginosa* (MTCC 1688) and *S. aureus* (MTCC 87) employing an amended Kirby Bauer technique. The cultures of all the test organisms were transferred to the nutrient broth (NB) at 37 °C

Table 1 Concentration of $AgNO_3$ solution used for the preparation of different ASN-SCS samples

$AgNO_3$ concentration (in mM)	Corresponding sample abbreviations
0.125	ASN-$SCS_{0.125}$
0.25	ASN-$SCS_{0.25}$
0.5	ASN-$SCS_{0.5}$
1	ASN-SCS_1
2	ASN-SCS_2
4	ASN-SCS_4
8	ASN-SCS_8
10	ASN-SCS_{10}
20	ASN-SCS_{20}
40	ASN-SCS_{40}
80	ASN-SCS_{80}
160	ASN-SCS_{160}
320	ASN-SCS_{320}

in a shaker-incubator operating at 150 rpm and left overnight. Thereafter, the cultures were diluted to 1×10^6 CFU mL^{-1}, and 200 μL of the diluted cells were spread on sterile Mueller–Hinton (MH) agar plates (100 × 6 mm) and amended with sterile ASN-SCS bandages around the edges ($d = 10.50 \pm 0.50$ mm) and kept overnight at 37 °C to record the inhibitory zones. The MH agar plates with only SCSs were also kept as a control set for comparison.

2.6.2 Bacterial growth inhibition kinetics. The bacterial growth inhibition kinetics were performed using *P. aeruginosa* (MTCC 1688). Overnight-grown *P. aeruginosa* (MTCC 1688) suspension (1%) was taken and inoculated into fresh MH broth containing different concentrations of ASN-SCSs, which were 0.125 mM, 0.25 mM, 0.5 mM, 1 mM, 8 mM, 80 mM, and 320 mM, respectively. The inoculated broths were then incubated at 37 °C in a shaker-incubator at 150 rpm. The bacterial growth was assessed at various time intervals by quantifying the O.D. at λ_{600} nm. The minimum inhibitory concentration (MIC), which refers to the lowest concentration of Ag NPs embedded in ASN-SCSs that inhibits visible bacterial growth, was also determined. Each experiment was conducted three times, and the mean values of the results were reported. MH broth containing bacterial inoculums without any ASN-SCS was used as the negative control, and MH broth containing ASN-SCS without any bacterial inoculum was used as the positive control.

2.6.3 Hemocompatibility analysis. The hemocompatibility of the ASN-SCS samples was evaluated through a hemolytic assay, as described previously.[50] A 0.4 mg mL^{-1} leaching aqueous solution of three samples of different ASN-SCSs (synthesized using 8 mM, 80 mM, and 320 mM $AgNO_3$ concentrations, respectively) was prepared. The aqueous dispersion was prepared through incubation of 0.4 mg mL^{-1} ASN-SCS in PBS solution at 37 °C for 24 h, 48 h, and 72 h, respectively. For the hemocompatibility assay, an EDTA-stabilized human blood sample was freshly collected. The diluted suspension of human red blood cells (RBCs, 0.4 mL) was then mixed with varied concentrations of ASN-SCSs (1.6 mL). Diluted suspensions of RBCs mixed with 1.6 mL of PBS and 1.6 mL of double-distilled water were used as negative and positive controls, respectively. The mixtures were incubated at room temperature for 2 h. The % hemolysis was calculated by measuring the absorbance of the supernatant at 541 nm in an UV-vis spectrophotometer (Varian Inc., USA) and using the following equation:

$$\%\ \text{hemolysis} = [(A_S - A_N)/(A_P - A_N)] \times 100$$

here, A_S, A_N, and A_P are the absorbances of the sample, negative control, and positive control, respectively. Moreover, RBCs present in the pellet are used to prepare smears and were examined under a microscope at a magnification of 400× to document any changes in the morphology of RBCs by ASN-SCSs.

2.6.4 MTT assay. Healthy human adult primary epidermal keratinocytes (HEKa) cells were seeded in 96-well microtiter plates with DMEM/F-12 medium and incubated at 37 °C in 5% CO_2 for 24 h. On the next day, a 0.4 mg mL^{-1} leaching aqueous solution of ASN-SCS_8, ASN-SCS_{80}, and ASN-SCS_{320} was prepared for three different time periods (24 h, 48 h, and 72 h) and added to each well, except the control, and kept further for incubation for another 24 hours at 37 °C in 5% CO_2. Subsequently, the plate was removed from the incubator, and the culture media were aspirated. Next, 10 μL of freshly prepared MTT reagent was added to each well and kept for 3 h under the same conditions. Afterward, 50 μL of isopropanol, a formazan solubilizer, was added to each well, and the absorbance was measured using an ELISA reader at 570 nm using a SPECTROstar Nano BMG LABTECH microtiter plate reader. All the factors such as dilution, mixing, trypsinization, *etc.*, were synchronized before calculating the cell viability. The cell viability percentage was determined using the formula:

$$[(\text{O.D. treated well} - \text{blank})/(\text{mean O.D. control well} - \text{blank})] \times 100.$$

2.6.5 Statistical analysis. All the triplicated data were analyzed using GraphPad Prism v. 8.4.2 and the values are presented as the mean ± standard deviation (SD).

3. Results and discussion

3.1 Preparation of SCS and ASN-SCS

During the preparation of SCS, the Eri cocoons were separated from exterior to interior into five segments, *i.e.*, cocoon coat (*i.e.*, floss), cocoon layers (*i.e.*, upper, middle, and lower layers), and cocoon lining (*i.e.*, pelade).[44] The cocoon coats, containing loose silk fibers along with discontinuous static air gaps, were discarded. Furthermore, non-mulberry cocoons possess better water exchange mobility than mulberry cocoons and, hence, are a potential candidate in biomedical applications,[51,52] especially in designing scaffold-based bandages. In Eri cocoons, the sericin content tends to decrease gradually from the outer to the inner layers.[53] Thus, the cocoon lining (pelade) with lower sericin content (5.95 ± 0.30%) and lower moisture regain capacity (11.94 ± 0.22%) was excluded from this study. Cocoon layers possessing the potential to qualify as a bandage material with higher sericin content (9.64 ± 0.47%) and higher moisture regain capacity (12.34

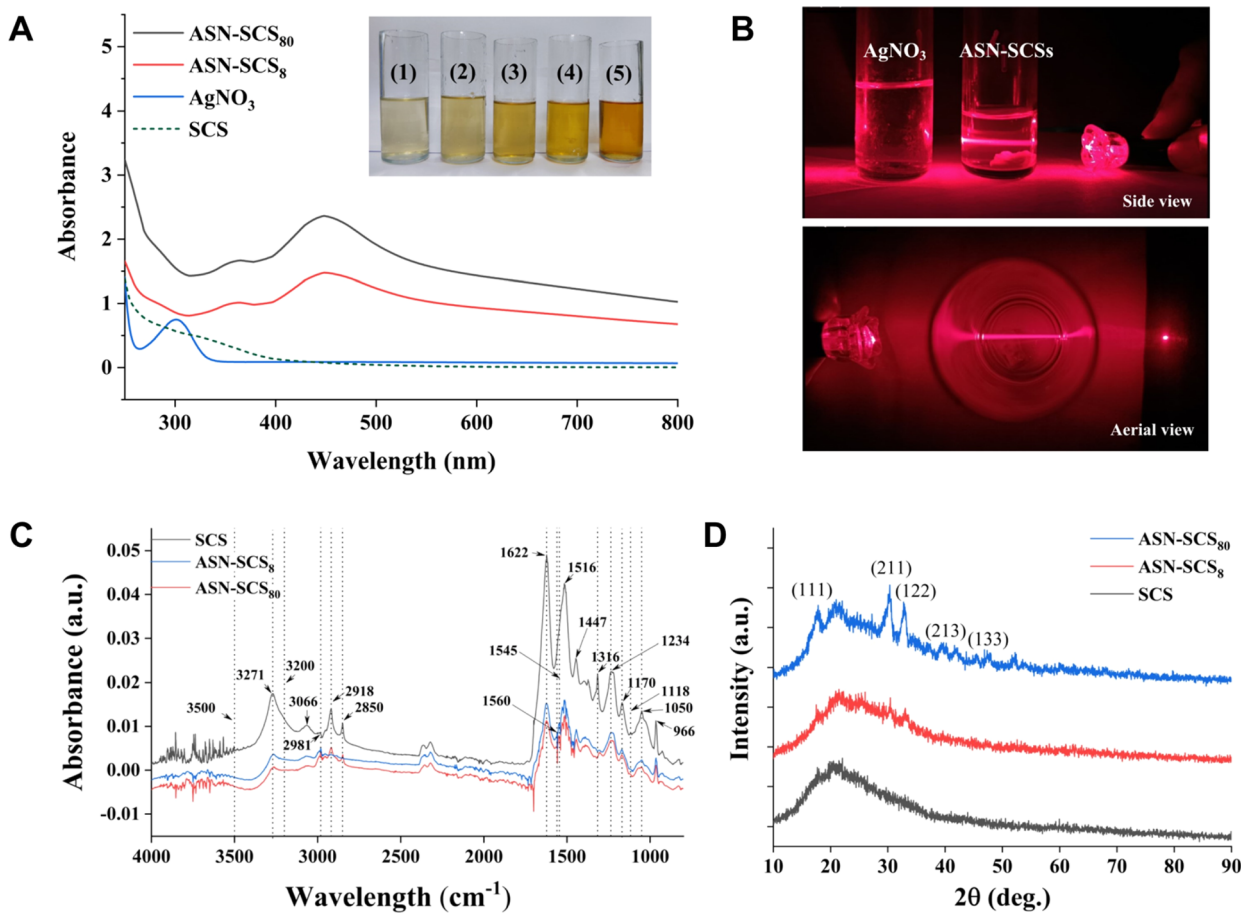

Fig. 2 (A) UV-vis absorption spectra of leached aqueous dispersions of ASN-SCSs in deionized water, $AgNO_3$ solution and Ajisawa solution during SCS synthesis. (B) Laser beam passing through aqueous solution of $AgNO_3$ and ASN-SCS solutions; upper image is side view, whereas the lower image is the aerial view. (C) FT-IR spectra of SCS and ASN-SCSs. (D) XRD analyses of SCS and ASN-SCSs.

± 0.31%) were screened for further processing. Ajisawa solution was utilized for partially dissolving fibroin molecules to obtain SCS, which was used for ASN-SCS synthesis and characterization.

3.2 Biophysical characterization

3.2.1 UV-vis spectroscopy and laser light scattering analyses. Once the Ajisawa solution altered its color (Fig. 2A inset), the solution was analyzed using a UV-vis spectrophotometer. It revealed no significant peak of sericin, suggesting that the majority of sericin content is retained in SCS and can potentially embed Ag NPs on their surface. The color variation in the Ajisawa solution was visualized due to the naturally occurring pigments present in the Eri cocoon structure as well as due to NP formation. UV-vis spectroscopy analyses of ASN-SCSs were used to inspect the reduction of Ag^+ ions to Ag^0. The light exposure causes the polarization of free electrons that conduct in Ag NPs, leading to electron dipolar oscillation and the development of a surface plasmon resonance (SPR) spectrum at 448 nm.[54] There was an absence of an absorption peak in the identical wavelength spectrum for the aqueous $AgNO_3$ solution that was used as a control. Fig. 2A presents the UV-vis absorption spectra of aqueous dispersions of ASN-SCSs containing Ag NPs. The laser beams passing through colloidal solution after the formation of ASN-SCSs exhibit the Tyndall effect of light scattering (Fig. 2B). The light scattering pattern due to the Tyndall effect preliminarily detects the formation of Ag NPs in the solution. The Tyndall effect was demonstrated with Ag NPs, which were microscopical colloidal particles yet sufficiently sized to scatter a light beam. The density of particles with colloidal structure and the frequency of the incident light both influence the magnitude of scattered light.

3.2.2 Fourier-transform infrared spectroscopy (FT-IR) analysis. The presence of a phenolic hydroxyl group in a molecule like tyrosine can typically exhibit characteristic peaks in the FTIR spectrum in the region between 3200 cm^{-1} and 3500 cm^{-1} due to the stretching vibration of the O–H bond.[55] The peaks of phenolic hydroxyl disappeared and were altered in the treated sample, indicating the interaction between the molecules and the NPs. Aromatic CH stretching vibrations usually appear as bands around 2800–3000 cm^{-1}. Bands at 2918 and 2850 cm^{-1} regions rising from stretching C–H of aromatic compounds were detected, which might participate in the synthesis process as capping agents or stabilizers. Hence, the weakening or disappearance in the intensity of these bands could reflect

alterations in the interactions between aromatic compounds and silver ions.[56] Moreover, in ASN-SCSs, the presence of a peak at 2981 cm^{-1} indicated the same.[57] The infrared spectral range across 1700 and 1500 cm^{-1} is frequently utilized for assessing diverse secondary features of silk fibroin. The peaks at 1610–1630 cm^{-1} and 1510–1520 cm^{-1} indicate the β-sheet secondary structure of silk fibroin, whereas the absorptions at 1648–1654 cm^{-1} and 1535–1542 cm^{-1} indicate the α-form conformation. The peaks at 1622 cm^{-1}, 1514 cm^{-1}, and 1236 cm^{-1} exhibit sericin amide-I (C=O stretching), amide-II (C–N stretching, N–H deformation), and amide-III (C–N stretching), suggesting a random coil/silk-I structure (Fig. 2C). The peak values at 1620–1625 cm^{-1} show C=O stretching of carboxylate ions,[58] whereas those at 1560 cm^{-1}, 1550–1545 cm^{-1}, and 1540 cm^{-1} denote association with silver–carboxylate complexes (–COO– + Ag). The development of large new absorption bands is due to NH deformation.[59] The peak at 1118 cm^{-1} reveals the stretching of the C–O bond of a phenolic hydroxyl group in the tyrosine of sericin. Following the reaction, the absorbance intensity at 1118 cm^{-1} weakens, indicating that the phenolic hydroxyl groups were cleaved and oxidized to create quinone structures. The strong vibration of 1316 cm^{-1} is assigned to the symmetric C=O stretching vibration of oxalate ions.[60] Here, the development of Ag NPs might be facilitated by the oxalate ions, which reduce Ag^{+} ions to Ag^{0} atoms. The peak at 1170 cm^{-1} corresponds to C–N stretching of tyrosine, and the intensity declined in the ASN-SCSs.[61] The band at 1050 cm^{-1} corresponds to sericin C–O stretching.[62]

3.2.3 X-ray diffraction (XRD) analysis. The analysis revealed the presence of silver peaks in the ASN-SCS samples. When the XRD graph was examined, there were characteristic peaks at positions $2\theta° = 17.668°$, 29.757°, 32.778°, 39.312°, and 47.835° assigned to the 111, 211, 122, 213 and 133 planes of crystalline Ag (JCPDS card no: 00-001-0856) (Fig. 2D). Ag NPs were crystallized, as the measured values closely correlated with the standard reference of the Joint Committee on Powder Diffraction Standards for Ag NPs. The strong and apparent peaks of the XRD spectrum suggested the crystalline structure of ASN-SCSs.

The particle size was determined using the line width of the XRD peak, *i.e.*, *hkl* data, using Debye–Scherrer's equation (Table 2). In the equation, wavelength of X-ray (λ), peak width, *i.e.*, full width at half of its maximum intensity in radians (β), angle between the incoming and outgoing beam directions (2θ), Bragg's diffraction angle (θ), Scherrer constant (K), and nanoparticle crystalline size or diameter ($D = K\lambda/\beta\cos\theta$) in nanometers.

Table 2 XRD data for the Debye–Scherrer equation (where $\lambda = 0.1541$ and $K = 0.9$) of ASN-SCSs

hkl	FWHM, deg	*B*, rad	2θ, deg	θ, deg	$\cos\theta$	D_{hkl}, nm
111	1.19455	0.02084	17.6680	8.8340	0.9881	6.65
211	1.08026	0.01885	29.7570	14.8785	0.9664	7.36
122	0.90165	0.01573	32.7780	16.3890	0.9593	8.82
213	1.40425	0.02450	39.3120	19.6560	0.9417	5.66
133	1.04384	0.01821	47.8350	29.9175	0.8667	7.62

The smallest NPs appeared to be primarily in their monocrystalline form. These characteristic peak values are consistent with previous reports.[16,63] An earlier study demonstrated that the bactericidal properties of Ag NPs within a range of 5–100 nm were dramatically increased as the NP size was reduced to <10 nm. This may be attributable to an elevation in the surface area to volume ratio (SA/V) with a reduction in particle size and an increase in relative particle concentration.[64]

3.2.4 SEM-EDX. SEM is a surface imaging technique that can determine the size, shape, and texture of particles. SEM images revealed the embedding of Ag NPs on the surface of ASN-SCSs (Fig. 3). Interestingly, ASN-SCS_{80} showed deposited NPs on silk that were absent in the control sample (SCS). The SCS, in turn, exhibits calcium oxalate crystals that got reduced on the ASN-SCS surface, indicating its role as a reducing agent during NP synthesis, which agrees with the FT-IR data. In an earlier report, a similar SEM study was performed to confirm nanosilica deposited on eri silk fabric.[65] Moreover, the EDX spectra of ASN-SCS revealed a percentage of Ag of 26.85%, which indicates that ASN-SCS was embedded with Ag NPs.

3.2.5 Thermogravimetric-differential thermal analysis (TGA/DTA). The thermal behavior and thermal stability of ASN-SCSs were investigated *via* TGA/DTA analysis at high temperatures (Fig. 4). The weight loss pattern in TGA curves can be categorized into three different regions depending on mass loss rates. The first region revealed a slight reduction in weight for silk scaffolds up to 110 °C, mostly due to water adsorption. The second zone (200–380 °C) showed a sharp increase in weight reduction, as most of the peptide chains were broken and intermolecular interactions decreased. The third zone, beginning at 380 °C, demonstrated a steady and persistent breakdown at a lower rate up to 800 °C. The final residual weight in control remained at 25.73% after 800 °C whereas, the remaining residual weight in treated samples (ASN-SCS_8 and ASN-SCS_{80}) was found to be 32.77% and 33.69%, respectively, which concludes enhanced stability of ASN-SCS bandages due to NPs embedded on SCS. Moreover, the stability of the ASN-SCS was much greater than previously reported studies, suggesting it as a durable bandage material for future biomedical applications.[66]

3.2.6 Hydrophilicity analysis. To measure the hydrophobicity of textiles, the water drop contact angle was measured. The surface becomes more hydrophobic when the water drop contact angle is >90° and superhydrophobic when the contact angle is >150°.[67] Fig. 5 shows the water contact angles of SCS and ASN-SCS. It depicts an increased contact angle as the percentage of embedded NPs increases in treated ASN-SCS relative to untreated SCS. The SCS exhibited a contact angle of 108.24°, which was raised to 123.63° in the case of ASN-SCS_{80}, indicating that both the samples are hydrophobic. Moreover, hydrophobicity intensified with increased NP deposition on ASN-SCS. An earlier study found that the roughness of the surface and the composition of its chemicals have a significant impact on the contact angle.[68] Aggregated NPs on the scaffold surface may enhance surface micro-roughness, potentially increasing fabric hydrophobicity because of the lotus effect.[69] Hence, the increased hydrophobicity of ASN-SCS, along with its

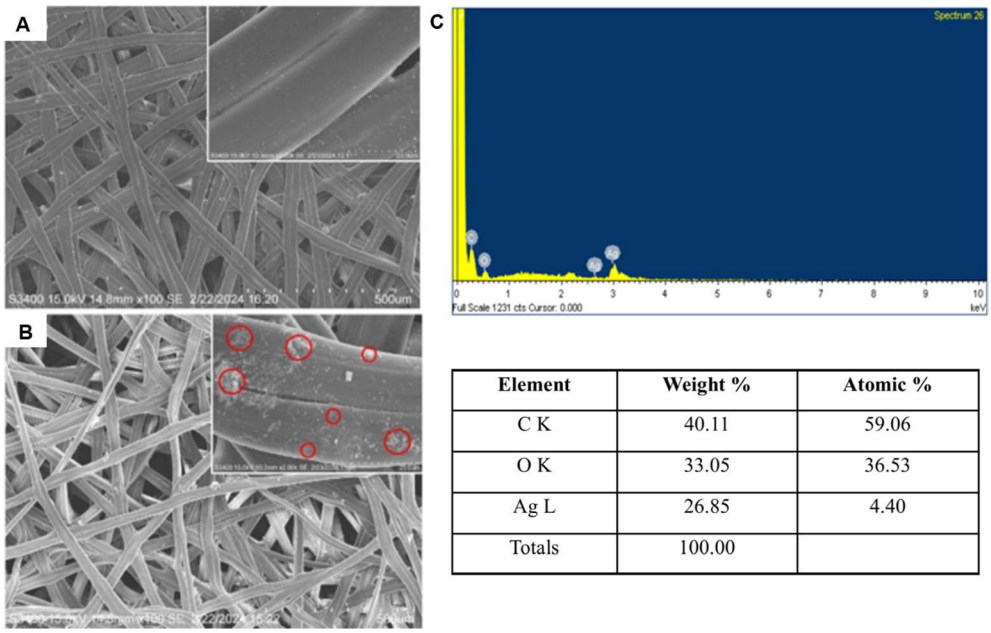

Element	Weight %	Atomic %
C K	40.11	59.06
O K	33.05	36.53
Ag L	26.85	4.40
Totals	100.00	

Fig. 3 SEM micrograph of (A) SCS and (B) ASN-SCS. Red circles in the inset of (B) indicate ASN-SCS embedded with NPs. (C) EDX spectrum of ASN-SCS.

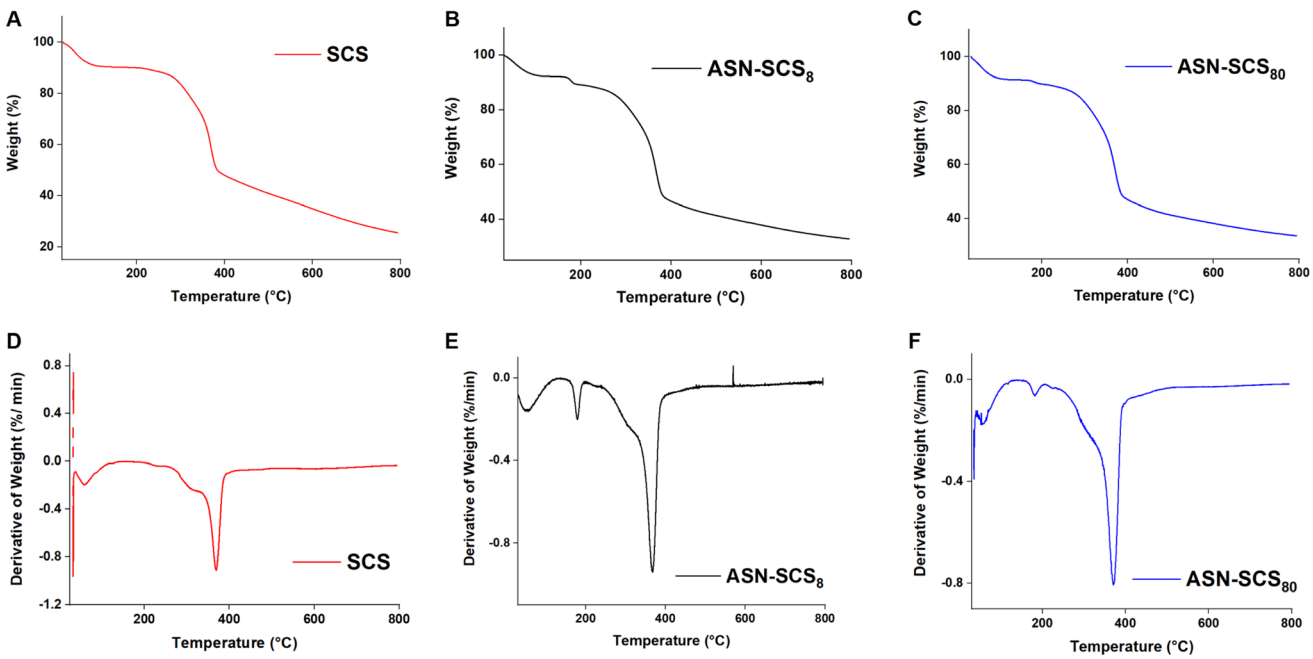

Fig. 4 The TGA/DTA curve of SCS and ASN-SCSs.

microstructured surface, is anticipated to inhibit biofilm formation in the case of one of the antibacterial actions of ASN-SCS. Generally, microbes have a lower ability to adhere to structured surfaces compared to flat films. This is because micro-structured surfaces minimize the amount of surface area accessible for microorganisms to adhere to.[70] Previous studies revealed that hydrophobic dressings could inhibit biofilm formation, leading to an adverse impact on antimicrobial resistance and promoting immune system mobilization.[71] As a result, synthesized ASN-SCS has the potential to be excellent wound dressing materials.

3.3 *In vitro* tests

3.3.1 Kirby–Bauer test of synthesized ASN-SCSs. The synthesized ASN-SCSs were investigated for antibacterial activity against two major burn wound-inhabiting multi-drug-

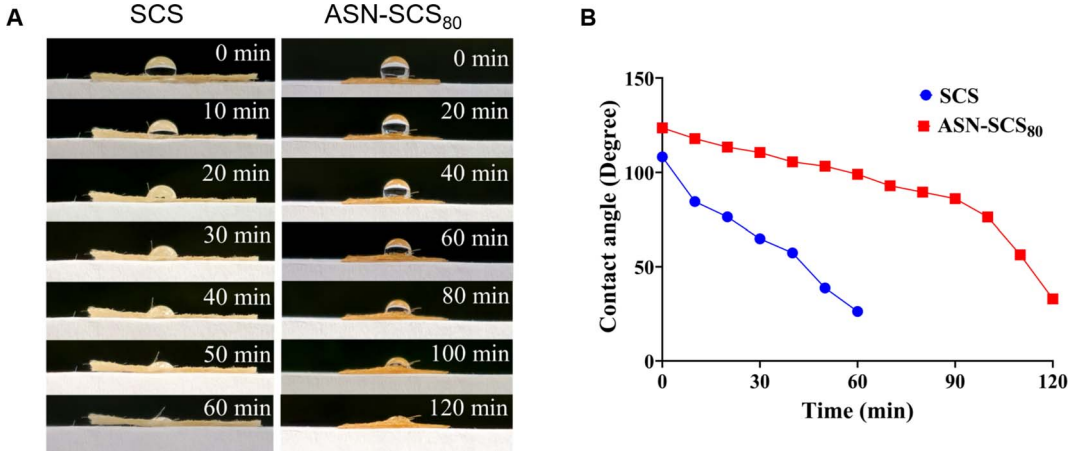

Fig. 5 (A) Time lapse photographs of water droplets on the SCS and ASN-SCS_{80}. (B) Contact angles of water droplets on the SCS and ASN-SCS_{80} as a function of time.

resistant pathogens: *P. aeruginosa* (MTCC 1688) and *Staphylococcus aureus* (MTCC 87). ASN-SCSs synthesized using three different cocoon layers [upper (1), middle (2), and lower (3)] exhibited strong antibacterial efficacy against these tested MDR pathogens with distinct inhibition zones (Fig. 6).

All the cocoon layers showed approximately similar inhibition zones when tested against either Gram-negative or Gram-positive bacteria. Therefore, utilizing multiple cocoon layers from the same cocoon would be economically beneficial for industrial use in the future. The antibacterial efficacy of the ASN-SCSs was slightly higher in Gram-negative bacteria when compared to the results of Gram-positive bacteria. The plausible explanation for these differential inhibition zones is connected to the fact that the cell walls of Gram-negative bacteria possess a thin layer of peptidoglycans. On the other hand, the likelihood of Ag NPs penetrating Gram-positive bacterial cells is reduced by their thick peptidoglycan coating. The antibacterial performance of ASN-SCSs prepared with varied concentrations of $AgNO_3$ was evaluated against *P. aeruginosa* (MTCC 1688), which is the major burn wound-colonizing bacteria (Fig. 6C–L). Following a 24 h incubation period at 37 °C, varying levels of antibacterial activity were seen in each sample, with the ASN-SCS prepared using an 80 mM concentration of $AgNO_3$ depicted as ASN-SCS_{80} clearly demonstrating the highest antibacterial zones (5.50 mm) against the tested bacterium. These results point to an improved antimicrobial efficacy at a lower dosage compared to previous reports where the highest zone of inhibition was observed for silkworm cocoon-based wound dressings synthesized using 200 mM of $AgNO_3$.[33] The control SCSs displayed no inhibition against *P. aeruginosa*, which suggests that silk has no antibacterial effect (Fig. 6M). It was previously stated that the chemical residues that remained after isolating or purifying the cocoon components were accountable for the antibacterial characteristics of pure silk cocoons.[72] However, in this study, the zone diameters of ASN-SCS samples gradually increased up to ASN-SCS_{80}; thereafter, they decreased, as noted for ASN-SCS_{160} and ASN-SCS_{320} (Fig. 6K and L). Thus, ASN-SCS_{80} was chosen for further study and large-scale production. The antibacterial effect of ASN-SCSs could be attributed to the release of Ag^+ from the sample discs, which resulted in increased antibacterial activity. In contrast, ASN-SCSs synthesized with higher $AgNO_3$ concentrations, *viz.*, ASN-SCS_{160} and ASN-SCS_{320}, exhibited a sharp decrease in the zone of inhibition which might be linked to the fact that the higher concentration of Ag NPs result in agglomeration as reported previously.[33] However, further study is needed to validate this.

3.3.2 Microbial growth inhibition study. The results of the Kirby Bauer test analysis revealed that the antibacterial effect is prominent in each sample of ASN-SCSs synthesized using 1, 2, 4, 8, 10, 20, 40, 80, 160, and 320 mM $AgNO_3$ solution. To explore the efficacy of these ASN-SCSs, the growth kinetics of *P. aeruginosa* were checked in the presence of ASN-SCSs, and the MIC value was estimated. The bacterial inhibition of the tested bacterium treated with ASN-SCSs (ASN-$SCS_{0.125}$ to ASN-SCS_{320}) was almost 100% when recorded after 24 h of incubation amended with 0.2 g of different concentrations of ASN-SCSs in a 20 mL bacterium culture broth with an initial O.D. of 0.06 at λ_{600} (Fig. 3A). Our results further showed that the bacterial inhibition from ASN-$SCS_{0.5}$ to ASN-SCS_{320} against *P. aeruginosa* was nearly 100% even after 72 h of incubation. Furthermore, MIC was also assessed to precisely determine the lowest concentration of ASN-SCSs, preventing the visible growth of *P. aeruginosa*. Among all the experimental sets, ASN-$SCS_{0.5}$ was depicted as the MIC value.

The bacterial population began proliferating after 24 h of incubation in broths treated with ASN-$SCS_{0.25}$ and ASN-$SCS_{0.125}$ due to delayed lag-phase (Fig. 7A) and degradation of silk proteins by the test bacterium to utilize the amino acids as a nitrogen source for its growth. Therefore, the released proteins might have contributed to the increased absorbance value in the ASN-$SCS_{0.125}$ sample. A similar interpretation was also described in a separate study where *P. aeruginosa* could potentially carry out silk biodegradation in minimal medium by proteolytic enzymes called elastases.[73] While most silk-

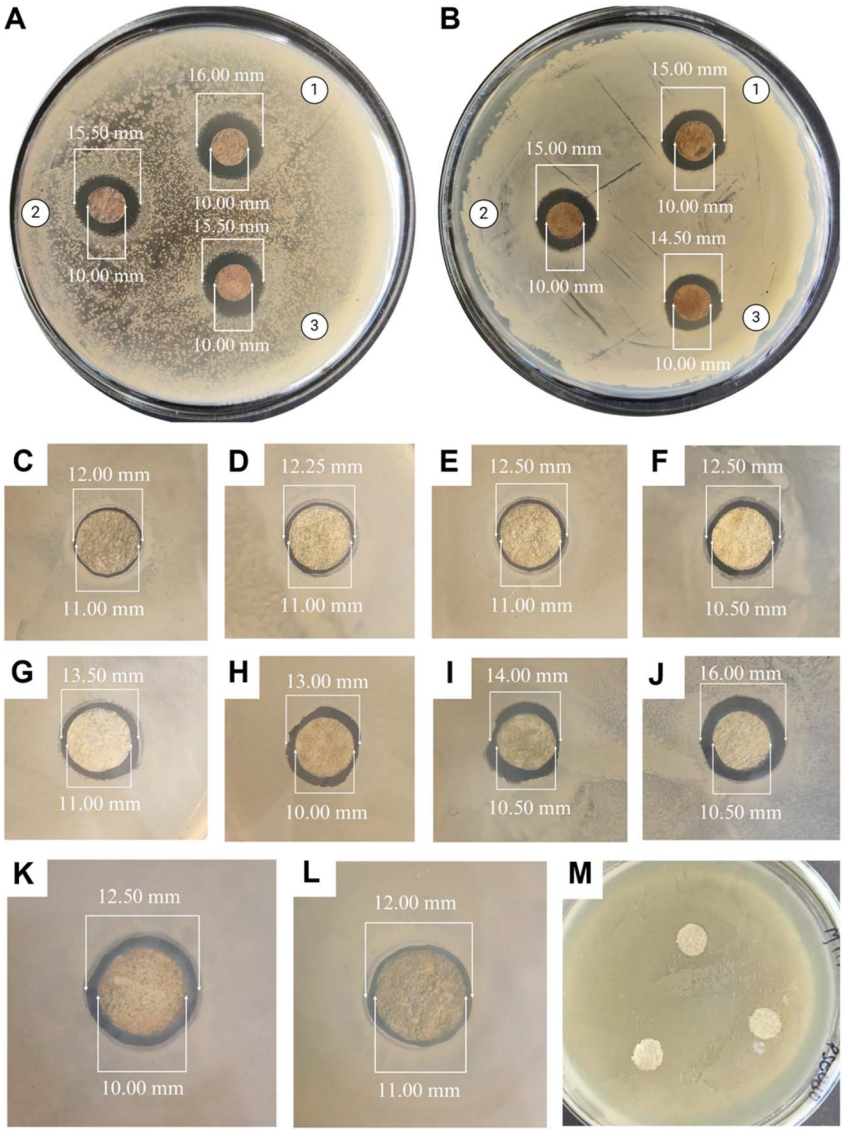

Fig. 6 Antibacterial assay of ASN-SCS (using 80 mM $AgNO_3$ abbreviated as ASN-SCS_{80}) synthesized using three different cocoon layers against (A) Gram negative bacteria *P. aeruginosa* and (B) Gram positive bacteria *S. aureus*; where the ASN-SCSs prepared utilizing upper, middle, and lower layers of Eri cocoons are indicated with 1, 2 and 3 respectively. Zone of inhibition diameters (in mm) of (C–L) ASN-SCSs synthesized using 1, 2, 4, 8, 10, 20, 40, 80, 160, 320 mM $AgNO_3$ solution respectively; and (M) SCSs as negative control against *P. aeruginosa*.

degrading gram negatives use sericin to obtain amino acids, another species of the genus *Pseudomonas* named *Burkholderia cepacia* (formerly *Pseudomonas cepacia*) was utilizing fibroin proteins as a nitrogen as well as carbon source. To visualize the morphological changes in ASN-SCS-treated bacteria, the SEM study was carried out, where the membrane stability was altered after ASN-SCS application, indicating the bactericidal effect of ASN-SCSs (Fig. 7A inset).

3.3.3 *In vitro* hemocompatibility analysis of ASN-SCSs. The hemolytic assay is a crucial test for any biomaterials that contact blood, assessing their hemocompatibility to determine their selection for further use. According to the ISO standard, a material is deemed safe if its hemolysis index is <5%.[74] The hemocompatibility analysis on human red blood cells was accomplished using the leaching aqueous dispersion of ASN-SCS bandages. Most of the samples exhibited <1% hemolysis, indicating their hemocompatible nature (Table 3, Fig. 7B).

The positive control-lysed RBCs exhibited two significant peaks in their absorption spectra (Fig. 7B). According to the literature, the two high absorption peaks in hemoglobin's (Hb) spectrum, nearly at 540 and 576 nm, along with an absorption valley at 560 nm, indicate that oxygen partial pressure (PO_2) is higher than 100 mm Hg and an oxy-Hb structure was formed.[75] Various studies have shown that silk bandages are hemocompatible. As well, dose-dependent Ag NPs do not have high hemolysis potential.[76] In our previous study, 13% hemolysis was observed in the presence of 40 μg mL^{-1} of bioconjugated Ag NPs.[77] Elsewhere, it was suggested that Ag NPs affect platelet aggregation, and blood coagulation over a concentration of 40

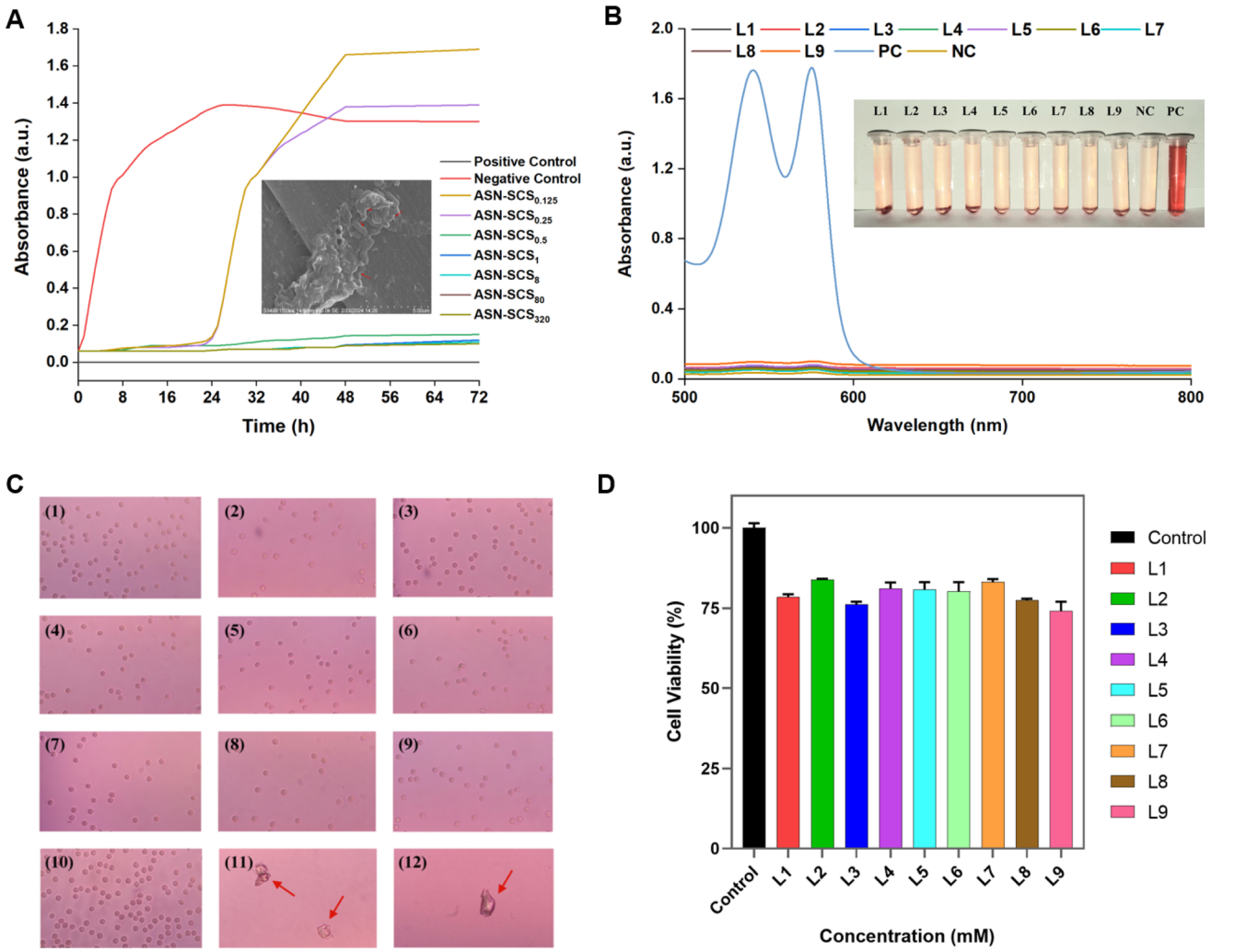

Fig. 7 (A) Growth kinetics of *P. aeruginosa* in the presence of different concentrations of Ag NPs embedded in ASN-SCSs for 72 h (ASN-ASN-$SCS_{0.125}$, ASN-$SCS_{0.25}$, ASN-$SCS_{0.5}$, ASN-SCS_1, ASN-SCS_8, ASN-SCS_{80}, and ASN-SCS_{320} denote ASN-SCSs prepared in 0.125 mM, 0.25 mM, 0.5 mM, 1 mM, 8 mM, 80 mM, and 320 mM $AgNO_3$ solution). Figure inset denotes the SEM micrograph of *P. aeruginosa* treated with ASN-SCSs; red arrows indicate changes in bacterial morphology. (B) Hemolysis study of human RBCs treated with varied concentrations of ASN-SCSs. RBCs suspended in PBS and distilled water were used as negative and positive controls, respectively. The inset represents the photographs of centrifuged samples, ensuring the supernatant contains no hemoglobin (Hb). (C) Microscopic images of RBCs present in blood smears prepared from samples L1–L9 (1–9), NC (10), and PC (11–12), containing ghost RBCs (red arrow). (D) Cell viability analysis using the MTT assay on HEKa cells. The results shown are the mean ± SD of three separate experiments performed in triplicate.

Table 3 Hemolysis assay of leaching liquors from different ASN-SCSs

ASN-SCSs	Leaching duration	Sample	% Hemolysis
ASN-SCS_8	24h	L1	0.14
ASN-SCS_{80}	24h	L2	0.45
ASN-SCS_{320}	24h	L3	0.63
ASN-SCS_8	48h	L4	0.15
ASN-SCS_{80}	48h	L5	0.57
ASN-SCS_{320}	48h	L6	0.81
ASN-SCS_8	72h	L7	0.61
ASN-SCS_{80}	72h	L8	0.94
ASN-SCS_{320}	72h	L9	1.88

μg mL^{-1}.[78] Despite synthesis with greater concentrations of $AgNO_3$, ASN-SCSs did not exhibit significant hemolysis (Fig. 7B, Table 3), indicating their hemocompatible nature, which supports their potential use in tissue engineering and wound healing. Moreover, blood smears prepared from the RBCs present in the sample pellet after final centrifugation during hemocompatibility analysis procedures revealed the presence of intact RBCs in all the samples. No significant changes in the shape and morphology of RBCs or in absorbance spectra (Fig. 7C) were recorded in the negative control. In turn, the positive control samples were composed of ghost RBCs.

3.3.4 MTT assay. To estimate the effect of the synthesized ASN-SCSs on humans, healthy human adult primary epidermal keratinocytes (HEKa) cells were used. The MTT assay relies on the respiratory system of the mitochondria and secondarily helps in the evaluation of the cellular energy capacity of a viable cell. MTT is a yellow dye that is reduced by oxido-reductase, where NADPH

serves as an electron donor, resulting in the blue-colored product, formazan. Such transformation is feasible only in live cells; thus, the amount of formazan is directly correlated to the number of viable cells. No cytotoxicity was detected, regardless of the leaching time of ASN-SCSs. The ASN-SCS_{80} exhibited high biocompatibility with a cell viability of approximately 80% (Fig. 7D), which agrees well with a previous study where silkworm cocoon wound film exhibited no significant cytotoxity against murine L929 fibroblast cells and the cell viability was > 80%.[33]

4. Conclusion

In conclusion, ASN-SCSs synthesized using eri silkworm cocoon were biomimetic, preserving both the benefits of fibroin and sericin, and qualified as an advanced dressing compared to conventional dressings. *In situ* assembly of Ag NPs on SCS was carried out using natural functional groups present in sericin and fibroin molecules as reducing and stabilizing agents. Moreover, the ASN-SCS bandages showed excellent thermal stability and water retention properties. The embedded Ag NPs exhibited a particle size ranging from 5.66 to 8.82 nm. ASN-SCSs were found to be strongly effective as an antibacterial agent against MDR pathogens, *i.e.*, against both *P. aeruginosa* and *S. aureus*. Following the demonstration of hemocompatibility *in vitro*, ASN-SCS bandages exhibited superior biocompatibility, which suggests their potential application in chronic wounds such as burns. Due to embedded Ag NPs, ASN-SCSs would possess an increased shelf life and remain sterile for a longer period, supporting less biomedical waste generation. As an outcome, this work presented an easy and sustainable way for developing a novel multifunctional bandage or dressing that has significant therapeutic potential in clinical and biomedical sectors. Therefore, this approach would substantially reduce production costs, simplify the fabrication process, and enable facile commercialization.

Data availability

The data supporting this article is included in the manuscript.

Author contributions

The manuscript was written through contributions of all authors. All authors have given approval to the final version of the manuscript.

Conflicts of interest

The authors declare no competing financial interest.

Acknowledgements

P. D. was provided with an independent Ph.D. fellowship for financial assistance (UGC-SRF; NTA Ref. No. 201610181190). R. M. would like to acknowledge the Department of Science & Technology, Government of India, for the DST-INSPIRE Ph.D. Fellowship (DST-INSPIRE-SRF; INSPIRE Code-IF190457). S. S. was provided with an independent Ph.D. fellowship (UGC-JRF; NTA Ref. No. 201610120606). A. K. M. acknowledges DST-SERB India for financial assistance (sanction order number: EEQ/2021/000058). Y. N. E. acknowledges financial support by 2232 International Fellowship for Outstanding Researchers Program of TÜBİTAK (project no: 118C346). We acknowledge Fatma Ozsoy for her contributions to the interpretation of the XRD data.

References

1 Y. N. Ertas, D. Ertas, A. Erdem, F. Segujja, S. Dulchavsky and N. Ashammakhi, Diagnostic, Therapeutic, and Theranostic Multifunctional Microneedles, *Small*, 2024, 2308479, DOI: 10.1002/smll.202308479.
2 O. A. Peña and P. Martin, Cellular and Molecular Mechanisms of Skin Wound Healing, *Nat. Rev. Mol. Cell Biol.*, 2024, 1–18, DOI: 10.1038/s41580-024-00715-1.
3 G. Kaur, G. Narayanan, D. Garg, A. Sachdev and I. Matai, Biomaterials-Based Regenerative Strategies for Skin Tissue Wound Healing, *ACS Appl. Bio Mater.*, 2022, **5**(5), 2069–2106, DOI: 10.1021/acsabm.2c00035.
4 C. Du, D. A. Fikhman, D. Persaud and M. B. B. Monroe, Dual Burst and Sustained Release of *p*-Coumaric Acid from Shape Memory Polymer Foams for Polymicrobial Infection Prevention in Trauma-Related Hemorrhagic Wounds, *ACS Appl. Mater. Interfaces*, 2023, **15**(20), 24228–24243, DOI: 10.1021/acsami.3c04392.
5 L. Xi, L. Wang, M. Zhang, C. He, X. Yang, Y. Pang, H. Chen and F. Cheng, TNF-R1 Cellular Nanovesicles Loaded on the Thermosensitive F-127 Hydrogel Enhance the Repair of Scalded Skin, *ACS Biomater. Sci. Eng.*, 2023, **9**(10), 5843–5854, DOI: 10.1021/acsbiomaterials.2c01257.
6 M. J. Hop, S. Polinder, C. H. Van Der Vlies, E. Middelkoop and M. E. Van Baar, Costs of Burn Care: A Systematic Review, *Wound Repair Regen.*, 2014, **22**(4), 436–450, DOI: 10.1111/wrr.12189.
7 W. Norbury, D. N. Herndon, J. Tanksley, M. G. Jeschke, C. C. Finnerty and on Behalf of the Scientific Study Committee of the Surgical Infection Society, Infection in Burns, *Surg. Infect.*, 2016, **17**(2), 250–255, DOI: 10.1089/sur.2013.134.
8 Z. Ma, J. Han, B. Chang, L. Gao, Z. Lu, F. Lu, H. Zhao, C. Zhang and X. Bie, Membrane-Active Amphipathic Peptide WRL3 with *In Vitro* Antibiofilm Capability and *In Vivo* Efficacy in Treating Methicillin-Resistant *Staphylococcus Aureus* Burn Wound Infections, *ACS Infect. Dis.*, 2017, **3**(11), 820–832, DOI: 10.1021/acsinfecdis.7b00100.
9 N. Agnihotri, V. Gupta and R. M. Joshi, Aerobic Bacterial Isolates from Burn Wound Infections and Their Antibiograms—A Five-Year Study, *Burns*, 2004, **30**(3), 241–243, DOI: 10.1016/j.burns.2003.11.010.
10 Y. Yang, J. Huang, A. Zeng, X. Long, N. Yu and X. Wang, The Role of the Skin Microbiome in Wound Healing, *Burns & Trauma*, 2024, **12**, tkad059, DOI: 10.1093/burnst/tkad059.

11 J. Li, S. Zhang, C. He and J. Ling, Electrospun Fibers Based Anisotropic Silk Fibroin Film with Photodynamic Antibacterial Therapy for *S. aureus* Infected Wound Healing, *Int. J. Biol. Macromol.*, 2024, **254**, 127685, DOI: 10.1016/j.ijbiomac.2023.127685.

12 S. Dabagh, S. A. Haris, B. K. Isfahani, N. Ashammakhi and Y. N. Ertas, Zeolite-Copper Ferrite Nanocomposites with Improved Antibacterial Activity and Reusability for Biomedical Applications, *ACS Appl. Nano Mater.*, 2023, **6**(22), 21412–21423, DOI: 10.1021/acsanm.3c05003.

13 J. Butler, R. D. Handy, M. Upton and A. Besinis, Review of Antimicrobial Nanocoatings in Medicine and Dentistry: Mechanisms of Action, Biocompatibility Performance, Safety, and Benefits Compared to Antibiotics, *ACS Nano*, 2023, **17**(8), 7064–7092, DOI: 10.1021/acsnano.2c12488.

14 N. Devi, Saima, S. K. Pandey, D. Kaur, V. Kumar, R. K. Sharma and N. Wangoo, Membrane Penetrating-Cationic Peptide BP100 Functionalized Silver Nanoparticles as Efficient Antibacterial Agents, *ACS Appl. Nano Mater.*, 2024, **7**(5), 4731–4741, DOI: 10.1021/acsanm.3c05159.

15 G. Shumi, T. B. Demissie, R. Eswaramoorthy, R. F. Bogale, G. Kenasa and T. Desalegn, Biosynthesis of Silver Nanoparticles Functionalized with Histidine and Phenylalanine Amino Acids for Potential Antioxidant and Antibacterial Activities, *ACS Omega*, 2023, **8**(27), 24371–24386, DOI: 10.1021/acsomega.3c01910.

16 S. Dabagh, S. A. Haris, B. K. Isfahani and Y. N. Ertas, Silver-Decorated and Silica-Capped Magnetite Nanoparticles with Effective Antibacterial Activity and Reusability, *ACS Appl. Bio Mater.*, 2023, **6**(6), 2266–2276, DOI: 10.1021/acsabm.3c00122.

17 F. Z. Moshfegh, M. M. Khoram and D. Nematollahi, Green Electrochemical Synthesis of Silver Sulfadiazine Microcrystals, *RSC Adv.*, 2019, **9**(42), 24105–24109, DOI: 10.1039/C9RA04504J.

18 R. Cartotto, Topical Antimicrobial Agents for Pediatric Burns, *Burns & Trauma*, 2017, **5**(33), 1–8, DOI: 10.1186/s41038-017-0096-6.

19 L. Rahman, Y. Sarwar, S. Khaliq, Inayatullah, W. Abbas, A. Mobeen, A. Ullah, S. Z. Hussain, W. S. Khan, M.-E. Kyriazi, I. Hussain, A. G. Kanaras and A. Rehman, Surfactin-Conjugated Silver Nanoparticles as an Antibacterial and Antibiofilm Agent against *Pseudomonas Aeruginosa*, *ACS Appl. Mater. Interfaces*, 2023, **15**(37), 43321–43331, DOI: 10.1021/acsami.3c07071.

20 P. Dam, M. Celik, M. Ustun, S. Saha, C. Saha, E. A. Kacar, S. Kugu, E. N. Karagulle, S. Tasoglu, F. Buyukserin, R. Mondal, P. Roy, M. L. R. Macedo, O. L. Franco, M. H. Cardoso, S. Altuntas and A. K. Mandal, Wound Healing Strategies Based on Nanoparticles Incorporated in Hydrogel Wound Patches, *RSC Adv.*, 2023, **13**(31), 21345–21364, DOI: 10.1039/D3RA03477A.

21 N. Tripathi and M. K. Goshisht, Recent Advances and Mechanistic Insights into Antibacterial Activity, Antibiofilm Activity, and Cytotoxicity of Silver Nanoparticles, *ACS Appl. Bio Mater.*, 2022, **5**(4), 1391–1463, DOI: 10.1021/acsabm.2c00014.

22 G. Tao, L. Liu, Y. Wang, H. Chang, P. Zhao, H. Zuo and H. He, Characterization of Silver Nanoparticle *In Situ* Synthesis on Porous Sericin Gel for Antibacterial Application, *J. Nanomater.*, 2016, **2016**, 1–8, DOI: 10.1155/2016/9505704.

23 I. Noreen, A. Hashmi, Y. Iqbal, F. P. Malik, M. Iqbal and F. Amin, In-Situ Formation of Azo Dye Capped-Silver Nanoparticles and Their Nanocomposite with Reduced Graphene Oxide for Dye Degradation, *Mater. Chem. Phys.*, 2023, **308**, 128299, DOI: 10.1016/j.matchemphys.2023.128299.

24 Md. A. Al Masud, H. Shaikh, Md. S. Alam, M. M. Karim, M. A. Momin, M. A. Islam and G. M. A. Khan, Green Synthesis of Silk Sericin-Embedded Silver Nanoparticles and Their Antibacterial Application against Multidrug-Resistant Pathogens, *J. Genet. Eng. Biotechnol.*, 2021, **19**(1), 74, DOI: 10.1186/s43141-021-00176-5.

25 S. Zhang, L. Yang, Y. Wang, G. Yang, Y. Li, Y. Li, J. Zhu, R. Li, W. Xie, Q. Wan, X. Pei, J. Chen, X. Zhang and J. Wang, Development of a Stretchable and Water-Resistant Hydrogel with Antibacterial and Antioxidant Dual Functions for Wound Healing in Movable Parts, *ACS Appl. Mater. Interfaces*, 2023, **15**(37), 43524–43540, DOI: 10.1021/acsami.3c08782.

26 P. Jayabal, V. Kannan Sampathkumar, A. Vinothkumar, S. Mathapati, B. Pannerselvam, S. Achiraman and G. D. Venkatasubbu, Fabrication of a Chitosan-Based Wound Dressing Patch for Enhanced Antimicrobial, Hemostatic, and Wound Healing Application, *ACS Appl. Bio Mater.*, 2023, **6**(2), 615–627, DOI: 10.1021/acsabm.2c00903.

27 Y. Wang, X. Wang, D. Zhou, X. Xia, H. Zhou, Y. Wang and H. Ke, Preparation and Characterization of Polycaprolactone (PCL) Antimicrobial Wound Dressing Loaded with Pomegranate Peel Extract, *ACS Omega*, 2023, **8**(23), 20323–20331, DOI: 10.1021/acsomega.2c08180.

28 M. Farahani and A. Shafiee, Wound Healing: From Passive to Smart Dressings, *Adv. Healthcare Mater.*, 2021, **10**(16), 2100477, DOI: 10.1002/adhm.202100477.

29 Q. Zeng, X. Qi, G. Shi, M. Zhang and H. Haick, Wound Dressing: From Nanomaterials to Diagnostic Dressings and Healing Evaluations, *ACS Nano*, 2022, **16**(2), 1708–1733, DOI: 10.1021/acsnano.1c08411.

30 V. Kumar, A. Kumar, N. S. Chauhan, G. Yadav, M. Goswami and G. Packirisamy, Design and Fabrication of a Dual Protein-Based Trilayered Nanofibrous Scaffold for Efficient Wound Healing, *ACS Appl. Bio Mater.*, 2022, **5**(6), 2726–2740, DOI: 10.1021/acsabm.2c00200.

31 Y. Deng, C. Yang, Y. Zhu, W. Liu, H. Li, L. Wang, W. Chen, Z. Wang and L. Wang, Lamprey-Teeth-Inspired Oriented Antibacterial Sericin Microneedles for Infected Wound Healing Improvement, *Nano Lett.*, 2022, **22**(7), 2702–2711, DOI: 10.1021/acs.nanolett.1c04573.

32 S. Zhang, W. Yang, W. Gong, Y. Lu, D.-G. Yu and P. Liu, Recent Progress of Electrospun Nanofibers as Burning Dressings, *RSC Adv.*, 2024, **14**(20), 14374–14391, DOI: 10.1039/D4RA01514B.

33 K. Yu, F. Lu, Q. Li, H. Chen, B. Lu, J. Liu, Z. Li, F. Dai, D. Wu and G. Lan, In Situ Assembly of Ag Nanoparticles (AgNPs) on

Porous Silkworm Cocoon-Based Wound Film: Enhanced Antimicrobial and Wound Healing Activity, *Sci. Rep.*, 2017, **7**(1), 2107, DOI: **10.1038/s41598-017-02270-6**.

34 R. Ramakrishnan, D. Chouhan, H. Vijayakumar Sreelatha, S. Arumugam, B. B. Mandal and L. K. Krishnan, Silk Fibroin-Based Bioengineered Scaffold for Enabling Hemostasis and Skin Regeneration of Critical-Size Full-Thickness Heat-Induced Burn Wounds, *ACS Biomater. Sci. Eng.*, 2022, **8**(9), 3856–3870, DOI: **10.1021/acsbiomaterials.2c00328**.

35 W. Zhang, L. Chen, J. Chen, L. Wang, X. Gui, J. Ran, G. Xu, H. Zhao, M. Zeng, J. Ji, L. Qian, J. Zhou, H. Ouyang and X. Zou, Silk Fibroin Biomaterial Shows Safe and Effective Wound Healing in Animal Models and a Randomized Controlled Clinical Trial, *Adv. Healthcare Mater.*, 2017, **6**(10), 1700121, DOI: **10.1002/adhm.201700121**.

36 R. Yu, Y. Yang, J. He, M. Li and B. Guo, Novel Supramolecular Self-Healing Silk Fibroin-Based Hydrogel via Host–Guest Interaction as Wound Dressing to Enhance Wound Healing, *Chem. Eng. J.*, 2021, **417**, 128278, DOI: **10.1016/j.cej.2020.128278**.

37 F. Munir, H. M. Tahir, S. Ali, A. Ali, A. Tehreem, S. D. E. S. Zaidi, M. Adnan and F. Ijaz, Characterization and Evaluation of Silk Sericin-Based Hydrogel: A Promising Biomaterial for Efficient Healing of Acute Wounds, *ACS Omega*, 2023, **8**(35), 32090–32098, DOI: **10.1021/acsomega.3c04178**.

38 S. Yan, J. Li, Y. Gao, J. You, S. Xu, C. Wang, Y. Yang and X. Wu, Encapsulation of Sericin-Decorated Efficient Agents in Silk Hydrogels for Wound Dressings, *ACS Appl. Mater. Interfaces*, 2023, **15**(42), 48952–48962, DOI: **10.1021/acsami.3c10044**.

39 K. Yazawa, K. Nakayama and Y. Gotoh, Silkworm Cocoon Waste Revitalization: Regenerated Fibers Using Higher-Molecular-Weight Fibroin Achieve High Strength and Toughness, *ACS Sustainable Chem. Eng.*, 2023, **11**(6), 2151–2159, DOI: **10.1021/acssuschemeng.2c05185**.

40 B. Blossman-Myer and W. W. Burggren, The Silk Cocoon of the Silkworm, Bombyx Mori: Macro Structure and Its Influence on Transmural Diffusion of Oxygen and Water Vapor, *Comp. Biochem. Physiol., Part A: Mol. Integr. Physiol.*, 2010, **155**(2), 259–263, DOI: **10.1016/j.cbpa.2009.11.007**.

41 M. Roy, S. K. Meena, T. S. Kusurkar, S. K. Singh, N. K. Sethy, K. Bhargava, S. Sarkar and M. Das, Carbon dioxide Gating in Silk Cocoon, *Biointerphases*, 2012, **7**(1), 45, DOI: **10.1007/s13758-012-0045-7**.

42 P. Dam, S. Altuntas, R. Mondal, J. R. V. Baudrit, A. Kati, S. Ghorai, A. Sadat, D. Gangopadhyay, S. Shaw, O. L. Franco, N. Temur, Y. N. Ertas, A. K. Mandal and I. Ocsoy, Silk-Based Nano-Biocomposite Scaffolds for Skin Organogenesis, *Mater. Lett.*, 2022, **327**, 133024, DOI: **10.1016/j.matlet.2022.133024**.

43 J. Zhang, J. Li, X. Jin, S. Du, J. Kaur and X. Wang, Natural and Highly Protective Composite Structures – Wild Silkworm Cocoons, *Compos. Commun.*, 2017, **4**, 1–4, DOI: **10.1016/j.coco.2017.02.005**.

44 D. Chattopadhyay, A. Chakraborty and S. M. Chatterjee, Microstructural Characteristics of Eri Silk Fibre in Different Layers of Cocoon, *J. Nat. Fibers*, 2023, **20**(1), 2146828, DOI: **10.1080/15440478.2022.2146828**.

45 G. Sabarees, G. P. Tamilarasi, V. Velmurugan, V. Alagarsamy, B. Z. Sibuh, M. Sikarwar, P. Taneja, A. Kumar and P. K. Gupta, Emerging Trends in Silk Fibroin Based Nanofibers for Impaired Wound Healing, *J. Drug Delivery Sci. Technol.*, 2023, **79**, 103994, DOI: **10.1016/j.jddst.2022.103994**.

46 M. Andiappan, T. Kumari, S. Sundaramoorthy, G. Meiyazhagan, P. Manoharan and G. Venkataraman, Comparison of Eri and Tasar Silk Fibroin Scaffolds for Biomedical Applications, *Prog. Biomater.*, 2016, **5**(2), 81–91, DOI: **10.1007/s40204-016-0047-5**.

47 J. Liu, L. Shi, Y. Deng, M. Zou, B. Cai, Y. Song, Z. Wang and L. Wang, Silk Sericin-Based Materials for Biomedical Applications, *Biomaterials*, 2022, **287**, 121638, DOI: **10.1016/j.biomaterials.2022.121638**.

48 M. Tamta and S. Mahajan, The Novel Silk Fiber: Eri, *Int. J. Home Sci.*, 2021, **7**(1), 101–104.

49 S. Li, L. Li, C. Guo, H. Qin and X. Yu, A Promising Wound Dressing Material with Excellent Cytocompatibility and Proangiogenesis Action for Wound Healing: Strontium Loaded Silk Fibroin/Sodium Alginate (SF/SA) Blend Films, *Int. J. Biol. Macromol.*, 2017, **104**, 969–978, DOI: **10.1016/j.ijbiomac.2017.07.020**.

50 J. Nesa, S. K. Jana, A. Sadat, K. Biswas, A. Kati, O. Kaya, R. Mondal, P. Dam, M. Thakur, A. Kumar, M. Hossain, L. R. Lima, S. B. Rezende, D. Bhattacharjya, D. Gangopadhyay, S. Ghorai, S. Altuntas, A. K. Panda, P. Chakrabarti, S. Swarnakar, J. Chakraborty, B. Yilmaz, M. L. R. Macedo, O. L. Franco, M. H. Cardoso and A. K. Mandal, Antimicrobial Potential of a Ponericin-like Peptide Isolated from Bombyx Mori L. Hemolymph in Response to *Pseudomonas aeruginosa* Infection, *Sci. Rep.*, 2022, **12**(1), 15493, DOI: **10.1038/s41598-022-19450-8**.

51 G. Janani, M. Kumar, D. Chouhan, J. C. Moses, A. Gangrade, S. Bhattacharjee and B. B. Mandal, Insight into Silk-Based Biomaterials: From Physicochemical Attributes to Recent Biomedical Applications, *ACS Appl. Bio Mater.*, 2019, **2**(12), 5460–5491, DOI: **10.1021/acsabm.9b00576**.

52 D. Naskar, S. Sapru, A. K. Ghosh, R. L. Reis, T. Dey and S. C. Kundu, Nonmulberry Silk Proteins: Multipurpose Ingredient in Bio-Functional Assembly, *Biomed. Mater.*, 2021, **16**(6), 062002, DOI: **10.1088/1748-605X/ac20a0**.

53 Z. Dong, Q. Xia and P. Zhao, Antimicrobial Components in the Cocoon Silk of Silkworm, *Bombyx Mori*, *Int. J. Biol. Macromol.*, 2023, **224**, 68–78, DOI: **10.1016/j.ijbiomac.2022.10.103**.

54 A. P. Ajaykumar, O. Sabira, M. Sebastian, S. R. Varma, K. B. Roy, V. S. Binitha, V. A. Rasheed, K. N. Jayaraj and A. R. Vignesh, A Novel Approach for the Biosynthesis of Silver Nanoparticles Using the Defensive Gland Extracts of the Beetle, Luprops Tristis Fabricius, *Sci. Rep.*, 2023, **13**(1), 10186, DOI: **10.1038/s41598-023-37175-0**.

55 F. Dai, Q. Zhuang, G. Huang, H. Deng and X. Zhang, Infrared Spectrum Characteristics and Quantification of OH Groups

in Coal, *ACS Omega*, 2023, **8**(19), 17064–17076, DOI: **10.1021/acsomega.3c01336**.

56 K. Jyoti, M. Baunthiyal and A. Singh, Characterization of Silver Nanoparticles Synthesized Using Urtica Dioica Linn. Leaves and Their Synergistic Effects with Antibiotics, *J. Radiat. Res. Appl. Sci.*, 2016, **9**(3), 217–227, DOI: **10.1016/j.jrras.2015.10.002**.

57 A.-R. Phull, Q. Abbas, A. Ali, H. Raza, S. J. Kim, M. Zia and I. Haq, Antioxidant, Cytotoxic and Antimicrobial Activities of Green Synthesized Silver Nanoparticles from Crude Extract of Bergenia Ciliata, *Futur. J. Pharm. Sci.*, 2016, **2**(1), 31–36, DOI: **10.1016/j.fjps.2016.03.001**.

58 F. Wu, J. Liu, Z. Yang, F. Li, Y. Xiang, Y. Pan and Z. Xue, Highly Stable Silicon Anode Enabled by a Water-Soluble Tannic Acid Functionalized Dual-Network Binder, *ACS Appl. Mater. Interfaces*, 2024, **16**(18), 23396–23405, DOI: **10.1021/acsami.4c03768**.

59 U. Bunyatova, M. B. Hammouda and J. Zhang, Novel Light-Driven Functional AgNPs Induce Cancer Death at Extra Low Concentrations, *Sci. Rep.*, 2021, **11**(1), 13258, DOI: **10.1038/s41598-021-92689-9**.

60 S. P. Chenakin, S. A. Alekseev and N. Kruse, X-Ray Photoelectron Spectroscopy and Diffuse Reflectance Infrared Fourier Transform Spectroscopy Insight into the Pathways of Manganese Oxalate Thermal Decomposition to MnO and $MnCO_3$, *Inorg. Chem.*, 2022, **61**(31), 12106–12117, DOI: **10.1021/acs.inorgchem.2c00672**.

61 N. Altangerel, B. W. Neuman, P. R. Hemmer, V. V. Yakovlev, A. V. Sokolov and M. O. Scully, A Novel Non-Destructive Rapid Tool for Estimating Amino Acid Composition and Secondary Structures of Proteins in Solution, *Small Methods*, 2024, **8**(7), 2301191, DOI: **10.1002/smtd.202301191**.

62 T. Karimi, F. Mottaghitalab, H. Keshvari and M. Farokhi, Carboxymethyl Chitosan/Sodium Carboxymethyl Cellulose/Agarose Hydrogel Dressings Containing Silk Fibroin/Polydopamine Nanoparticles for Antibiotic Delivery, *J. Drug Delivery Sci. Technol.*, 2023, **80**, 104134, DOI: **10.1016/j.jddst.2022.104134**.

63 M. Ghaffarlou, A. Mohammadi, N. Mousazadeh, M. Salehiabar, Y. Kalantari, J. Charmi, M. Barsbay, Y. N. Ertas, H. Danafar, H. Rezaeejam, H. Nosrati and S. Javani, Facile Preparation of Silver Based Radiosensitizers via Biomineralization Method for Enhanced in Vivo Breast Cancer Radiotherapy, *Sci. Rep.*, 2023, **13**(1), 15131, DOI: **10.1038/s41598-023-40763-9**.

64 S. Agnihotri, S. Mukherji and S. Mukherji, Size-Controlled Silver Nanoparticles Synthesized over the Range 5–100 Nm Using the Same Protocol and Their Antibacterial Efficacy, *RSC Adv.*, 2014, **4**(8), 3974–3983, DOI: **10.1039/C3RA44507K**.

65 M. P. Borah, S. Jose, B. B. Kalita, D. Shakyawar and P. Pandit, Water Repellent Finishing on Eri Silk Fabric Using Nano Silica, *J. Text. Inst.*, 2020, **111**(5), 701–708, DOI: **10.1080/00405000.2019.1659470**.

66 G. Tao, R. Cai, Y. Wang, L. Liu, H. Zuo, P. Zhao, A. Umar, C. Mao, Q. Xia and H. He, Bioinspired Design of AgNPs Embedded Silk Sericin-Based Sponges for Efficiently Combating Bacteria and Promoting Wound Healing, *Mater. Des.*, 2019, **180**, 107940, DOI: **10.1016/j.matdes.2019.107940**.

67 S. Zhang, L. Zhao, M. Yu, J. Guo, C. Liu, C. Zhu, M. Zhao, Y. Huang and Y. Zheng, Measurement Methods for Droplet Adhesion Characteristics and Micrometer-Scale Quantification of Contact Angle on Superhydrophobic Surfaces: Challenges and Opportunities, *Langmuir*, 2024, **40**(19), 9873–9891, DOI: **10.1021/acs.langmuir.3c03967**.

68 A. Kumar Verma and A. Govind Rajan, Surface Roughness Explains the Observed Water Contact Angle and Slip Length on 2D Hexagonal Boron Nitride, *Langmuir*, 2022, **38**(30), 9210–9220, DOI: **10.1021/acs.langmuir.2c00972**.

69 Q. Yuan, C. Shi and T. He, SiO_2/TiO_2 and PDMS Modified Self-Cleaning Coating and Its Application in Decorative UHPC Surface, *Ceram. Int.*, 2024, **50**(4), 6194–6206, DOI: **10.1016/j.ceramint.2023.11.338**.

70 M. Mu, S. Liu, W. DeFlorio, L. Hao, X. Wang, K. S. Salazar, M. Taylor, A. Castillo, L. Cisneros-Zevallos, J. K. Oh, Y. Min and M. Akbulut, Influence of Surface Roughness, Nanostructure, and Wetting on Bacterial Adhesion, *Langmuir*, 2023, **39**(15), 5426–5439, DOI: **10.1021/acs.langmuir.3c00091**.

71 C. He, B. Yu, Y. Lv, Y. Huang, J. Guo, L. Li, M. Chen, Y. Zheng, M. Liu, S. Guo, X. Shi and J. Yang, Biomimetic Asymmetric Composite Dressing by Electrospinning with Aligned Nanofibrous and Micropatterned Structures for Severe Burn Wound Healing, *ACS Appl. Mater. Interfaces*, 2022, **14**(29), 32799–32812, DOI: **10.1021/acsami.2c04323**.

72 J. Kaur, R. Rajkhowa, T. Afrin, T. Tsuzuki and X. Wang, Facts and Myths of Antibacterial Properties of Silk, *Biopolymers*, 2014, **101**(3), 237–245, DOI: **10.1002/bip.22323**.

73 A. Diez-Galán, R. Cobos, A. Ibañez, C. Calvo-Peña and J. J. R. Coque, Biodegradation of Pine Processionary Caterpillar Silk Is Mediated by Elastase- and Subtilisin-like Proteases, *Int. J. Mol. Sci.*, 2022, **23**(23), 15253, DOI: **10.3390/ijms232315253**.

74 H. Nosrati, M. Salehiabar, J. Charmi, K. Yaray, M. Ghaffarlou, E. Balcioglu and Y. N. Ertas, Enhanced In Vivo Radiotherapy of Breast Cancer Using Gadolinium Oxide and Gold Hybrid Nanoparticles, *ACS Appl. Bio Mater.*, 2023, **6**(2), 784–792, DOI: **10.1021/acsabm.2c00965**.

75 P. Liu, Z. Zhu, C. Zeng and G. Nie, Specific Absorption Spectra of Hemoglobin at Different PO_2 Levels: Potential Noninvasive Method to Detect PO_2 in Tissues, *J. Biomed. Opt.*, 2012, **17**(12), 125002, DOI: **10.1117/1.JBO.17.12.125002**.

76 A. Bera, P. Ghosh, K. Goswami and P. De, Amino Acid-Based Polymer-Coated Silver Nanoparticles as Insulin Fibril Inhibitors, *ACS Appl. Nano Mater.*, 2023, **6**(10), 8705–8716, DOI: **10.1021/acsanm.3c01078**.

77 I. K. Sen, A. K. Mandal, S. Chakraborti, B. Dey, R. Chakraborty and S. S. Islam, Green Synthesis of Silver Nanoparticles Using Glucan from Mushroom and Study of Antibacterial Activity, *Int. J. Biol. Macromol.*, 2013, **62**, 439–449, DOI: **10.1016/j.ijbiomac.2013.09.019**.

78 H. Huang, W. Lai, M. Cui, L. Liang, Y. Lin, Q. Fang, Y. Liu and L. Xie, An Evaluation of Blood Compatibility of Silver Nanoparticles, *Sci. Rep.*, 2016, **6**(1), 25518, DOI: **10.1038/srep25518**.